# Tay creep: a multi-mechanism model for rate-dependent deformation of soils

ZHENHAO SHI*†, DAVID MUIR WOOD‡, MAOSONG HUANG*† and JAMES P. HAMBLETON§

Constitutive models constructed within the combined framework of kinematic hardening and bounding surface plasticity have proved to be successful in describing the rate-independent deformation of soils under non-monotonic histories of stress or strain. Most soils show some rate-dependence of their deformation characteristics, and it is important for the constitutive models to be able to reproduce rate- or time-dependent patterns of response. This paper explores a constitutive modelling approach that combines multiple viscoplastic mechanisms contributing to the overall rate-sensitive deformation of a soil. A simple viscoplastic extension of an inviscid kinematic hardening model incorporates two viscoplastic mechanisms applying an overstress formulation to a 'consolidation surface' and a 'recent stress history surface'. Depending on the current stress state and the relative 'strength' of the two mechanisms, the viscoplastic mechanisms may collaborate or compete with each other. This modelling approach is shown to be able to reproduce many observed patterns of rate-dependent response of soils.

KEYWORDS: elasto-viscoplasticity; kinematic hardening; soils; rate dependence; constitutive model

## INTRODUCTION

The time- and rate-dependent behaviour of soils has been extensively observed, including loading rate effects (Leroueil *et al.*, 1985; Sheahan *et al.*, 1996; Matsushita *et al.*, 1999), undrained and drained creep (Bjerrum, 1967; Campanella & Vaid, 1974; Tavenas *et al.*, 1978), and stress relaxation (Graham *et al.*, 1983; Hicher, 2016). Appropriate characterization and modelling of these viscous behaviours have been shown to be critical for solving geotechnical engineering problems related to the long-term performance of infrastructure (Oldecop & Alonso, 2007; Karstunen & Yin, 2010; Kelly *et al.*, 2018) and the prevention and mitigation of geohazards (Zhu & Randolph, 2011; Alonso *et al.*, 2016). Accordingly, many rate-dependent constitutive models have been developed for soils (Adachi & Oka, 1982; di Prisco & Imposimato, 1996; Kutter & Sathialingam, 1992; Leoni *et al.*, 2008; Yuan & Whittle, 2018), by means of overstress theory (Perzyna, 1963), isotache method (Suklje, 1957) or equivalent timeline (Bjerrum, 1967).

These existing models have been found to be effective in replicating the observed viscous characteristics of soils under monotonic histories of stresses or strains. However, the rate-sensitive behaviour of soils subjected to complex loading can be more intricate. Noticeable examples include delayed initiation of creep and temporary reversal of creep direction after rapid stress reduction (Hunsche, 1988; Lade *et al.*, 2009) and the dependence of the sign of creep and stress relaxation on the most recent change in effective stress (e.g., loading, unloading or reloading) (Pham Van Bang *et al.*, 2007; Maranha *et al.*, 2016; Hicher, 2016).

The peculiar soil behaviour described above creates challenges for existing constitutive laws, as the latter typically employ a single viscoplastic mechanism. The goal of this work is to formulate a multi-mechanism viscoplastic model and demonstrate that with two viscoplastic mechanisms these enigmatic observations can be anticipated. This modelling framework can be seen as the viscoplastic equivalent of inviscid elasto-plastic models rooted in the frameworks of multi-surface plasticity or nested-surface plasticity (Al-Tabbaa & Muir Wood, 1989; De Borst, 1986; Houlsby, 1999; Puzrin & Houlsby, 2004) and rate-dependent behaviour of other types of solids (Besson, 2009; Chaboche, 2008), where a number of independent yield surfaces or viscoplastic mechanisms are defined, giving rise to separate plastic strain components and contributing to the overall inelastic strains. It should be emphasized that the proposed framework differs from existing viscoplastic bounding surface models (e.g., Dafalias (1982); Kaliakin & Dafalias (1990); Shi *et al.* (2019)) in that the latter models consider only a *single* viscoplastic mechanism.

## MULTI-MECHANISM VISCOPLASTIC SOIL MODEL

This section presents a simple multi-mechanism viscoplastic model based on the rate-independent Modified Cam-clay

---

2

(MCC) model. The proposed model hereafter will be referred to as the *Tay creep* model (the city of Dundee sits on the River Tay). For simplicity, the model is presented with reference to triaxial stress conditions, in which the mean normal stress $p = (\sigma_a + 2\sigma_r)/3$ and deviatoric stress $q = \sigma_a - \sigma_r$ are stress measures, and the volumetric strain $\epsilon_p = \epsilon_a + 2\epsilon_r$ and deviatoric strain $\epsilon_q = 2(\epsilon_a - \epsilon_r)/3$ are the work-conjugate strain measures. Subscripts $a$ and $r$ denote axial and radial components, while $p$ and $q$ denote volumetric and deviatoric terms, respectively. All the stress quantities are regarded as effective stresses, and compression is assumed positive for both stress and strain measures.

The presented model rests on the following general strain rate decomposition:

$$\dot{\epsilon}_p = \dot{\epsilon}_p^e + \dot{\epsilon}_p^{vp}; \quad \dot{\epsilon}_q = \dot{\epsilon}_q^e + \dot{\epsilon}_q^{vp}; \tag{1}$$

Superscripts $e$ and $vp$ stand for elastic and viscoplastic, respectively, and the superposed dot indicates a time derivative. In its present form, the Tay creep model considers two mechanisms. A framework that extends the model to more than two mechanisms is described in the Appendix. Following classical viscoplasticity (Perzyna, 1963), the viscoplastic strain rate for each mechanism is computed by a viscosity function and a flow direction:

$$\dot{\epsilon}_p^{vp} = \langle \Phi^{\mathrm{I}} \rangle R_p^{\mathrm{I}} + \langle \Phi^{\mathrm{II}} \rangle R_p^{\mathrm{II}};$$
$$\dot{\epsilon}_q^{vp} = \langle \Phi^{\mathrm{I}} \rangle R_q^{\mathrm{I}} + \langle \Phi^{\mathrm{II}} \rangle R_q^{\mathrm{II}}; \tag{2}$$

where Macaulay brackets $\langle \rangle$ indicate $\langle x \rangle = x$ if $x \geq 0$ and $\langle x \rangle = 0$ if $x < 0$. In Eq. (2), $\Phi$ is the viscosity function, while $R_p$ and $R_q$ denote respectively the volumetric and deviatoric components of the flow direction. Superscripts I and II indicate the quantities associated with the first and second mechanisms, respectively.

*Viscosity function and flow direction*

We postulate that the mechanisms I and II in Eq. (2) describe the viscoplastic deformation related, respectively, to the consolidation or preloading of the soil and the recent stress history of the soil. The corresponding viscosity functions are defined through overstress (Perzyna, 1963) measured between the current stress and the centres of a consolidation surface ($F = 0$) and a recent stress history (RSH) surface ($f = 0$), as depicted in Fig. 1. Note that the two surfaces should not be interpreted as physical entities in stress space but rather geometric references that assist in defining continuous fields of viscosity functions for both mechanisms.

The consolidation surface assumes the same shape as that of the yield surface of the Modified Cam-clay model (Roscoe & Burland, 1968):

$$F = \bar{q}^2 - M^2 \bar{p}(p_0 - \bar{p}) = 0 \tag{3}$$
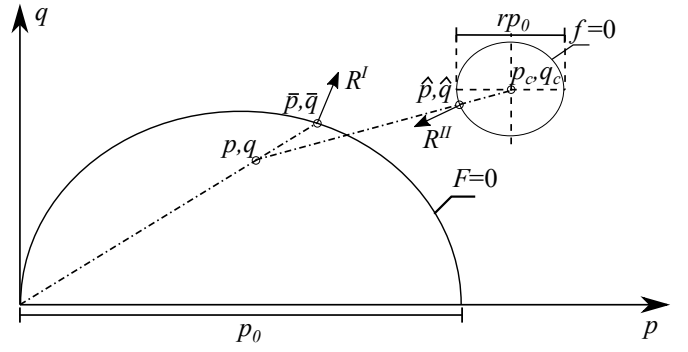
**Fig. 1. Schematics showing the definition of the consolidation surface $F = 0$, the recent stress history (RSH) surface $f = 0$, image stresses $(\bar{p}, \bar{q})$ and $(\hat{p}, \hat{q})$, and viscoplastic flow directions $R^{\mathrm{I}}$ and $R^{\mathrm{II}}$.**

where $M$ is the stress ratio at critical state and $p_0$ is an internal variable controlling the surface size. The variables $\bar{p}$ and $\bar{q}$ are image stresses projected from the origin of stress space through the current stress $(p, q)$, as illustrated in Fig. 1. Under such radial mapping (Dafalias, 1986), the image stress can be related to the current stress by

$$\bar{p} = b_F p \quad \bar{q} = b_F q \tag{4}$$

We use the quantity $1/b_F$ to measure the degree of overstress in relation to the consolidation surface, so that $1/b_F$ increases continuously as the current stress approaches the surface $F = 0$ from its interior, passes it, and moves away from it. We define $\Phi^{\mathrm{I}}$ through a classical power law:

$$\Phi^{\mathrm{I}} = \mu^{\mathrm{I}} \left(\frac{1}{b_F}\right)^{n^{\mathrm{I}}} \tag{5}$$

where $\mu^{\mathrm{I}}$ and $n^{\mathrm{I}}$ are material constants. The flow direction for mechanism I is assumed to be the gradient of $F = 0$ at the image stress (i.e., the unit vector $R^{\mathrm{I}}$ in Fig. 1):

$$R_p^{\mathrm{I}} = \frac{\bar{p}(M^2 - \bar{\eta}^2)}{\sqrt{\bar{p}^2(M^2 - \bar{\eta}^2)^2 + 4\bar{q}^2}};$$
$$R_q^{\mathrm{I}} = \frac{2\bar{q}}{\sqrt{\bar{p}^2(M^2 - \bar{\eta}^2)^2 + 4\bar{q}^2}}; \tag{6}$$

where $\bar{\eta}$ is the image stress ratio (i.e., $\bar{\eta} = \bar{q}/\bar{p} = \eta = q/p$).

The RSH surface is given the same shape as the consolidation surface and is described by

$$f = \frac{(\hat{q} - q_c)^2}{M^2} + (\hat{p} - p_c)^2 - (rp_0)^2 = 0 \tag{7}$$

where $(p_c, q_c)$ is the center of the surface. The size of this surface is indicated by $rp_0$, where $r$ is assumed to be a material constant. This assumption implies that the sizes of the consolidation surface and the RSH surface are coupled. This provides a simple route to model the way in which density hardening reduces the viscoplastic strains associated with either mechanism. The consequences of alternative modelling

choices—in particular uncoupling the two surfaces, perhaps by fixing the size of the RSH surface—could usefully be explored. The stress state $(\hat{p}, \hat{q})$ is a second image stress projected from the center of the RSH surface through the current stress onto the RSH surface (see Fig. 1), and its components are expressed as

$$\hat{p} = b_f(p - p_c) + p_c \quad \hat{q} = b_f(q - q_c) + q_c \quad (8)$$

Similar to the first mechanism, the viscosity function for the second mechanism is defined through the variable $b_f$:

$$\Phi^{\text{II}} = \mu^{\text{II}}(\frac{1}{b_f})^{n^{\text{II}}} \quad (9)$$

where $\mu^{\text{II}}$ and $n^{\text{II}}$ are material constants. The flow direction is a unit vector collinear with the gradient of the RSH surface at $(\hat{p}, \hat{q})$:

$$R_p^{\text{II}} = \frac{\hat{p} - p_c}{\sqrt{(\hat{p} - p_c)^2 + (\hat{q} - q_c)^2/M^4}};$$
$$R_q^{\text{II}} = \frac{(\hat{q} - q_c)/M^2}{\sqrt{(\hat{p} - p_c)^2 + (\hat{q} - q_c)^2/M^4}}; \quad (10)$$

*Hardening rules*

The model contains three internal variables: $p_0$, $p_c$, and $q_c$. The first one governs the isotropic hardening of both surfaces. Following the Cam-clay model (Schofield & Wroth, 1968; Roscoe & Burland, 1968), the increment of the surface size $dp_0$ is related to the increment of volumetric viscoplastic strain $d\epsilon_p^{vp}$ by

$$dp_0 = \frac{1}{\lambda^* - \kappa^*} p_0 d\epsilon_p^{vp} \quad (11)$$

where the parameters $\lambda^*$ and $\kappa^*$ denote the slope of normal compression line (NCL) and swelling line in $\ln p - \ln v$ space, respectively ($v$ is specific volume). Note that the hardening law of Eq. (11) implies that the evolution in size of the consolidation surface (also the RSH surface; see Eq. (7)) is attributed to the *total* irrecoverable volumetric strains contributed by both mechanisms. By employing such a hypothesis, we effectively treat $p_0$ as a macroscopic indication of the current microstructure of the soil, whose evolution, following classical critical state soil mechanics (Schofield & Wroth, 1968; Muir Wood, 2004), is driven by volume changes regardless of underlying mechanisms. Consequently, the combination of Eq. (11) and the hypoelastic model introduced in the next section (Eqs. (13) and (14)) defines a backbone normal compression behaviour, based on which isotaches that correspond to different loading rates are constructed (see Fig. 2).

We adopt a simple kinematic hardening rule to describe the translation of the RSH surface:

$$dp_c = \langle \Phi^{\text{II}} \rangle C(\hat{p} - p_c)dt$$
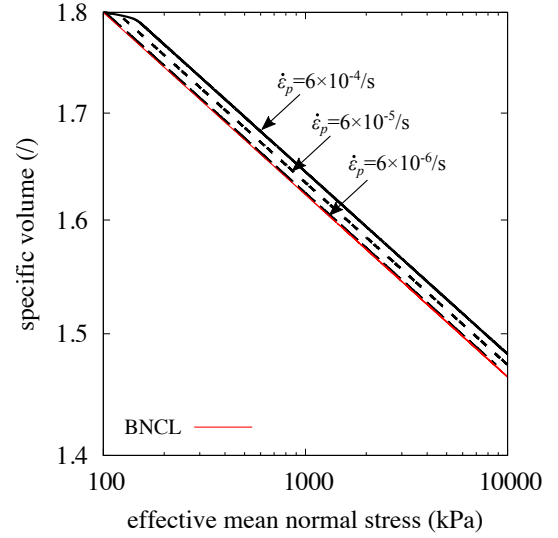$$dq_c = \langle \Phi^{\text{II}} \rangle C(\hat{q} - q_c)dt \quad (12)$$



**Fig. 2. Computed isotropic compression lines under different volumetric strain rates and the backbone normal compression line (BNCL) constructed in accordance with** $d\epsilon_p = \lambda^* dp/p$. **Model simulations are based on parameter set 1 in Table 1.**

where $C$ is a material constant that controls the strength of the kinematic hardening. The relation of Eq. (12) indicates that the centre of the RSH surface is attracted by the current stress state (recall that the direction pointing from the surface centre $(p_c, q_c)$ to the image stress state $(\hat{p}, \hat{q})$ is collinear with that pointing from $(p_c, q_c)$ to the current stress; see Fig. 1). Moreover, it is seen from Eq. (12) that we postulate that translation of the RSH surface is driven solely by mechanism II. The consequences of this modelling choice and alternative hypotheses will be evaluated with reference to experimental evidence in the following. Lastly, it should be noted that the RSH surface can move freely in stress space without restrictions: intersection of the two surfaces is permitted (cf. Mróz (1967); Prévost (1977); Al-Tabbaa & Muir Wood (1989); Rouainia & Muir Wood (2000)). Since the viscosities defined through the surfaces are continuous fields in stress space, the concept of intersection is irrelevant.

*Elastic model*

The proposed model is completed with an isotropic hypoelastic model as commonly assumed in many constitutive models:

$$\dot{p} = K\dot{\epsilon}_p^e; \quad \dot{q} = 3G\dot{\epsilon}_q^e \quad (13)$$

The elastic bulk modulus $K$ and shear modulus $G$ are evaluated as

$$K = \frac{p}{\kappa^*}; \quad G = \frac{3(1 - 2\nu)}{2(1 + \nu)}K \quad (14)$$

where $\nu$ denotes the Poisson's ratio.

*Model parameters and calibration*

The Tay creep model requires 10 constants (see Table 1). All can be calibrated from conventional soil laboratory tests (e.g., oedometer tests and triaxial tests) that include at least

one unloading-reloading cycle, during which creep or stress relaxation can be initiated. In particular, the constants $\kappa^*$, $\nu$, $\lambda^*$, and $M$ are classical Cam-clay parameters and thus can be calibrated following established procedures (e.g., Muir Wood (2004); Dafalias *et al.* (2006)). The constant $C$ controls the kinematic hardening of the RSH surface and defines a backbone stress-strain relation for unloading and reloading, where the current stress is located inside the consolidation surface and the consolidation mechanism is suppressed. The latter is because of the power-law viscosity function of Eq. (5) and typically large value of the power $n^{\mathrm{I}}$. The aforementioned backbone relation can be determined by performing slow-rate straining or tracking the ultimate stress or strain states attained during creep and stress relaxation, respectively, that are initiated during unloading or reloading. The parameter $r$ controls the size of the RSH surface, and hence, together with the constants $n^{\mathrm{II}}$ and $\mu^{\mathrm{II}}$, governs the intensity of the viscoplastic deformations associated with the RSH mechanism. Given the interactions between these parameters, we suggest fixing $r$ to a relatively small value (e.g., $r = 0.05 \sim 0.06$), while adjusting $n^{\mathrm{II}}$ and $\mu^{\mathrm{II}}$ in accordance with the temporal variations of stress or strain during creep or stress relaxation initiated during unloading or reloading stages (i.e., when the consolidation mechanism is largely suppressed). Similarly, the determination of $\mu^{\mathrm{I}}$ and $n^{\mathrm{I}}$, which control the strength of the viscoplastic mechanism I, is most suitably performed by matching the creep or stress relaxation initiated during primary loading that is mainly controlled by mechanism I. The parameter $n^{\mathrm{I}}$ can also be estimated by knowing conventional virgin compression index $C_c$, recompression index $C_r$, and secondary compression index $C_\alpha$ (Vermeer & Neher, 1999).

## INTERACTION BETWEEN VISCOPLASTIC MECHANISMS

Depending on the current state, the two viscoplastic mechanisms can interact differently. Broadly, the mechanisms can either 'compete' or 'collaborate'. These two forms of interplay are the keys to understanding the characteristics of soil behaviour simulated by the Tay creep model (see next section). As illustrated in Fig. 3(a), when the current stress rests on the opposite sides of the surfaces $F = 0$ and $f = 0$, the two mechanisms produce competing viscoplastic strains because the flow directions $R^{\mathrm{I}}$ and $R^{\mathrm{II}}$ in the figure point in opposite directions, and the overall inelastic response results from the competition between the two mechanisms. This competitive interaction is more likely to occur following a rapid change of loading direction, where the RSH mechanism more reactively aligns the flow direction with the the new loading direction (see $R^{\mathrm{II}}$ and $(\Delta p, \Delta q)$ in Fig. 3(a)), while the consolidation mechanism is more stable and not affected by the most recent stress history. Figure 3(b) illustrates the case of the collaboration between the two viscoplastic mechanisms. It can be seen that when the current stress lies on the same side of the
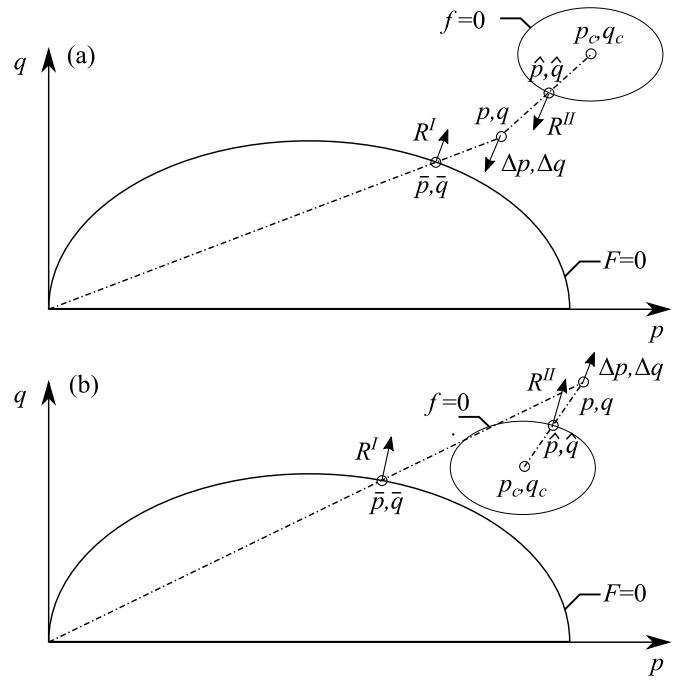


Fig. 3. Schematics showing the different interaction forms between the two viscoplastic mechanisms: (a) competition; (b) collaboration.

two surfaces, viscoplastic strain rates associated with the two mechanisms reinforce each other.

## CHARACTERISTICS OF THE TWO-MECHANISM VISCOPLASTIC MODEL

Typical responses simulated by the Tay creep model will be presented in this section, in order to highlight the behavioural characteristics produced by considering multi-mechanism viscoplasticity. Experimental evidence will also be presented to assess qualitatively whether such simulations are reasonable or useful. Model parameters employed are summarised in Table 1. Set 1 is chosen to replicate typical rate effects and 'isotache' deformation pattern observed for soils, and sets 2 to 4 are determined through calibration based on experimental data from laboratory tests. The constitutive model is implemented by using the integration algorithm proposed by Bardet & Choucair (1991), which linearises the loading constraints of laboratory experiments and relates them to the constitutive relations through a linear system of ordinary differential equations. This system is solved by explicit Runge-Kutta method with automatic error control (Tamagnini *et al.*, 2000).

*Typical rate-dependent behaviour and attainment of critical states*

Fig. 4 shows that the model reproduces the strain rate effects and 'isotache' behaviour typically observed for fine-grained soils (Graham *et al.*, 1983). Critical state is attained at relatively large shear strains. It should be noted that coarse-grained soils can exhibit a non-isotache pattern of response when strain

**Table 1. Material constants of two-mechanism viscoplastic model (sets 1 is used to simulate typical strain rate-dependent behaviour and the attainment of critical states; sets 2, 3 and 4 are calibrated for a crushed coral sand (Lade _et al._, 2009), Formacao de Benfica stiff clay (Maranha _et al._, 2016) and a saturated compacted clay (Hicher, 2016), respectively.)**

| parameters (unit) | set 1 | set 2 | set 3 | set 4 |
|---|---|---|---|---|
| $\kappa^*$ (/) | 0.005 | 0.002 | 0.002 | 0.01 |
| $\nu$ (/) | 0.17 | 0.25 | 0.173 | 0.15 |
| $\lambda^*$ (/) | 0.045 | 0.019 | 0.045 | 0.092 |
| $M$ (/) | 1.06 | 1.85 | 1.059 | 1.07 |
| $r$ (/) | 0.055 | 0.06 | 0.2 | 0.055 |
| $C$ (/) | $10 \times 10^3$ | $7 \times 10^3$ | $0.8 \times 10^3$ | $1.2 \times 10^3$ |
| $\mu^{\mathrm{I}}$ (s$^{-1}$) | $1 \times 10^{-6}$ | $1 \times 10^{-6}$ | $1 \times 10^{-7}$ | $1.67 \times 10^{-6}$ |
| $n^{\mathrm{I}}$ (/) | 15 | 16 | 15 | 25 |
| $\mu^{\mathrm{II}}$ (s$^{-1}$) | $1 \times 10^{-6}$ | $1 \times 10^{-6}$ | $1 \times 10^{-7}$ | $1.67 \times 10^{-6}$ |
| $n^{\mathrm{II}}$ (/) | 15 | 25 | 15 | 25 |
| initial internal variables (unit) | set 1 | set 2 | set 3 | set 4 |
| $p_0$ (kPa) | 100 | 200 | 567 | 400 |
| $p_c$ (kPa) | 100 | 200 | 420 | 400 |
| $q_c$ (kPa) | 0 | 0 | 250 | 0 |

rate is changed stepwise. As reported by Matsushita _et al._ (1999), Pham Van Bang _et al._ (2007), and Lade _et al._ (2009), stepwise changes in strain rate only temporarily alter the stress-strain response before rejoining the original curve. The modeling of this transient viscous behaviour by using Tay creep model might require the inclusion of other elements such as dynamic development and loss of structure or bonding (Cazacliu & Ibraim, 2016) or decaying viscosity (Yuan & Whittle, 2018; Pham Van Bang _et al._, 2007).

_Creep following rapid stress drop_

Creep following stress drop is a special test to explore the time-dependent characteristics of geomaterials (Hunsche, 1988; Lade _et al._, 2009), where soils are allowed to creep following a rapid reduction of stresses. Figs. 5 and 6 show the results of such a test on crushed coral sands during drained triaxial compression (Lade _et al._, 2009). The model simulations given in these figures are based on the parameter set 2 in Table 1. Among them, the constant $M$ is estimated from the ultimate stress ratio at large strains (approximately 18%) attained in drained triaxial compressions under constant strain rates (Lade _et al._, 2009), while the parameters $\kappa^*$, $\lambda^*$ and $\mu^{\mathrm{I}}$ are adjusted to fit the stress-strain and volume change that correspond to drained compression shear at an axial strain rate of 0.106%/min, as shown in Fig. 5. The parameters $n^{\mathrm{II}}$ is constrained by fitting the initial creep rate, while $n^{\mathrm{I}}$ and $C$ are determined by matching the maximum positive and negative axial strains developed during creep. The model simulations are found to be insensitive to the constant $\mu^{\mathrm{II}}$, which is then assumed to be $1 \times 10^{-6}$ s$^{-1}$. The initial value of $p_0$ is set to the effective mean normal stress prior to shearing, as normally the loading rate during consolidation is slow enough to allow the effective stress to lie on the consolidation surface. The centre of RSH surface takes the initial effective stress for the same reason mentioned above.

Fig. 5 shows that the model can reasonably represent many important aspects of measured soil response. In particular,
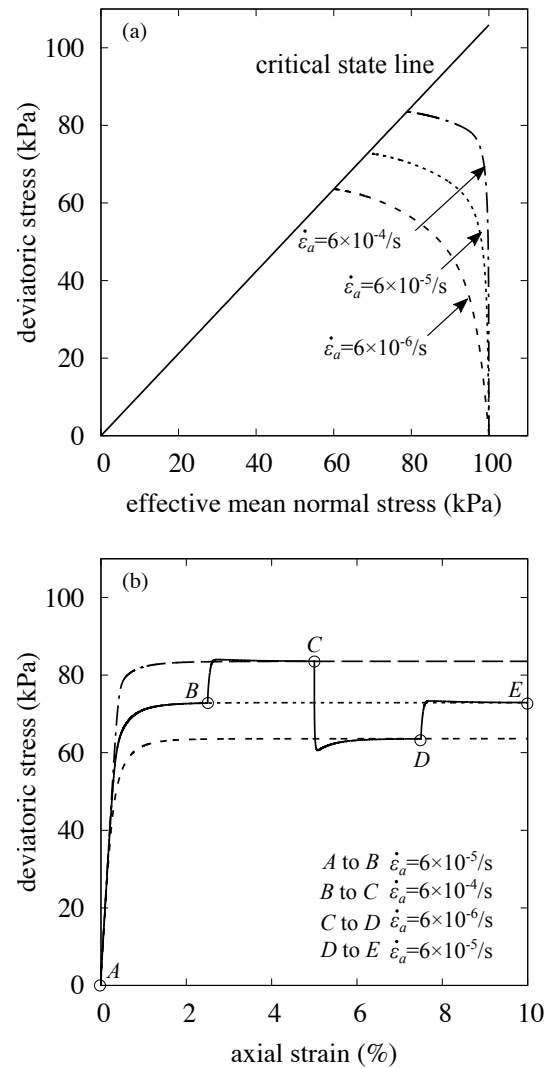


**Fig. 4. Simulation of constant-strain-rate undrained triaxial compression on clay-like soils (set 1 in Table 1) and test with step changes in axial strain rate: (a) effective stress paths; (b) stress-strain relationships. Note that distinctive stress-strain curves exist for each strain rate and step changes in strain rate take the stress-strain response to the new curve appropriate for that strain rate.**
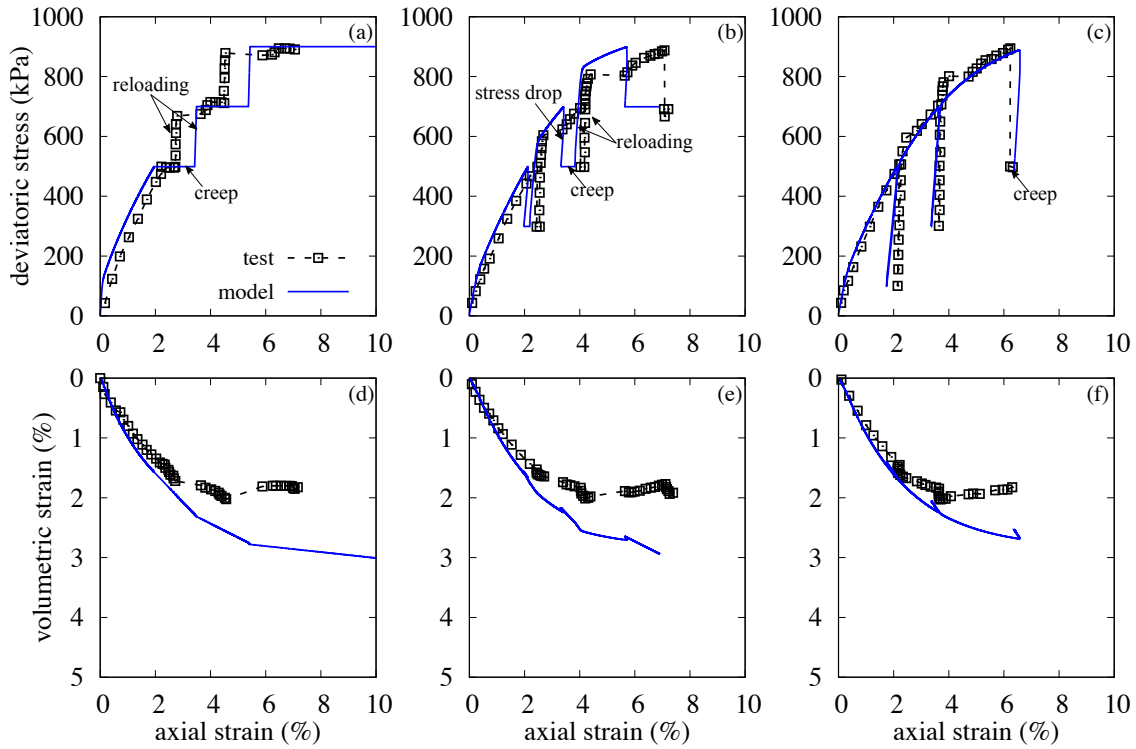
**Fig. 5.** Measured and computed response of crushed coral sand from drained triaxial compression with creep stages: (a) and (d) stress-strain and volume change relationships when creep is initiated with no stress drop; (b) and (e) creep is initiated following $\triangle q = -200$ **kPa stress drop; (c) and (f) creep is initiated following $\triangle q = -400$ kPa stress drop. The drained shear is initiated from an effective hydrostatic stress of 200 kPa and conducted at an average strain rate of 0.106 %/min. Each creep stage lasts for 1440 mins (Lade *et al.*, 2009).**

under given shear stresses, the creep initiated following stress drops (see the part labelled by "creep" in Fig. 5(b) and (c)) is noticeably smaller than that initiated during monotonic primary loading. The ageing effects of creep, as reflected by the nearly vertical stress-strain curve upon reloading and apparently overshooting the original primary loading relationships, are replicated by the model (see the part labelled by "reloading" in Fig. 5(a) and (b)). However, quantitative mismatches exist between test data and model computations. For instance, the model tends to overestimate the amount of creep deformation and shear-induced volume change. There are evidently discrepancies which result from the central role given to a Cam-clay like formulation, whereas for coarse-grained soils an extended Mohr-Coulomb model might be expected to provide the core of the creep model (Gajo & Muir Wood, 1999).

Fig. 6(a) and (b) present the computed and measured (Lade *et al.*, 2009) variations of axial strains with time (creep) after deviatoric stress has been rapidly reduced by 200 kPa and 400 kPa, respectively (i.e., the tests shown in Fig. 5(b) and (c)). The variable $q_{max}$ denotes the deviatoric stresses reached just before the drops. The test results show that a mild stress drop delays the initiation of creep deformation (see Fig. 6(a)), while a strong stress drop temporarily reverses the deformation direction (see Fig. 6(b)). This transient reversal of creep direction is captured by the proposed model through the interaction of the two independent viscoplastic mechanisms. Specifically, sudden stress drops locate the current stress on the

opposite sides of the two surfaces (i.e., the scenarios illustrated in Fig. 3(a)) and thus trigger the two mechanisms with opposite plastic flow directions. Initially, the RSH mechanism dominates the creep thus the straining direction is aligned with the most recent change in stress states (i.e., the correspondence between the decrease in axial strains and unloading). With the fading of the RSH mechanism as the RSH surface translates towards the current stress, the mechanism associated with the consolidation surface starts to dominate the creep process thus resulting in overall straining that is aligned with the primary loading.

Theoretically, if the two competing mechanisms were able to reach an equilibrium from the beginning, a postponed creep initiation, as observed in the experiments with mild stress reduction (see Fig. 6(a)), could be anticipated from the model. Nevertheless, based on our calibration, the model still predicts a transient reversal of straining direction, although the magnitude of 'negative' strain is small (i.e., see the inset figure in Fig. 6(a)). Further investigations and more experimental evidence are required to explore this mismatch. Fig. 6(c) and (d) emphasizes that the observed temporary reversal of creep direction cannot be replicated by considering only the consolidation mechanism.

To illustrate the effects of $C$—the key parameter that influences the RSH mechanism—Fig. 7 depicts a parametric study referring to the creep test with $\triangle q = -400$ kPa and $q_{max}$ = 900 kPa (i.e., Fig. 6(b)). The baseline corresponds to the calibrated set of parameters. The inset sketches the location of the RSH surface relative to the current stress. Based on this

spatial configuration of stress states and Eq. (12), lowering $C$ results in a 'slower' movement of the RSH surface towards the current stress and larger overstresses associated with the RSH surface, and hence the soil develops greater negative axial strains.

*Cyclic loading interrupted by creep*

Cyclic creep is another unconventional test that can be used to examine the influences of recent stress changes on the viscous behaviour of soils. Fig. 8 depicts such a test where undrained creep is initiated at various stages within an undrained unloading-reloading cycle (Maranha *et al.*, 2016). We use the two-mechanism model to simulate such a test, and the corresponding model parameters are listed as set 3 of Table 1. The Cam-clay parameters $\kappa^*$, $\lambda^*$, $\nu$ and $M$ are those reported by Maranha *et al.* (2016), while the constant $C$ is constrained by the need to fit the baseline stress-strain relationships during unloading (i.e., the collection of the creep states that correspond to the full development of delayed plasticity). The parameters $\mu^{\mathrm{I}}$ and $\mu^{\mathrm{II}}$ are adjusted based on the deformations attained at the end of each creep stage, and the constants $n^{\mathrm{I}} = n^{\mathrm{II}} = 15$ are assumed. Note that the parameter $r$ adopts a relatively large value compared with other examples, which is found necessary for generating significant creep deformation during unloading stage. The initial value of $p_0$ is estimated by assuming that the consolidation surface passes through the initial stress state prior to unloading (i.e., it is assumed that the rate of primary loading is sufficiently slow to allow the effective stress states to lie on the consolidation surface). For the same reason, the centre of the RSH is assumed to coincide with the initial stress state.

Fig. 8 shows that the model reasonably represents the most important features observed in the test: the direction of creep deformation is aligned with that of the most recent stress history (i.e. the creep initiated following unloading exhibits decreasing axial strains while that activated during reloading shows increasing axial deformation); and the magnitude of creep increases as the unloading/reloading proceeds. As discussed in the previous section, the two viscoplastic mechanisms interact competitively while the soil is unloaded. The unloading-induced deterioration of the mechanism associated with consolidation results in growing creep deformation aligned with the RSH. On the other hand, the two mechanisms collaborate during reloading, as sketched in Fig. 3(b), and the strengthening of the consolidation mechanism due to reloading contributes to an increase in the positive creep deformation. There are some aspects of the experiments that are, however, not replicated by the model in its current form. For instance, the experimental data show that creep associated with decreasing axial strains can be observed as early as following the first unloading phase (i.e., see the part circled in Fig. 8(b)), while the model computation suggests that the consolidation mechanism still dominates this stage and hence axial strains increase. Moreover, the computed relative increase in time-dependent

deformation between consequent creep during later unloading stages is smaller than that observed. Lastly, the test data indicate that excess pore pressure decreases during creep initiated during reloading, while the computation shows that the pore pressure increases. These mismatches can be closely related to the translation of the RSH surface and consequently its relation with the current stress. Future model improvements, therefore, might be pursued by replacing the current simple kinematic hardening rule with more sophisticated translation laws and/or including more intermediate viscoplastic mechanisms as will be explained later.

We use the cyclic creep test discussed above as an opportunity to explore the consequences of some alternative modelling choices. As shown in Fig. 9(a), if only the consolidation mechanism is active (i.e., we set the parameter $\mu^{\mathrm{II}} = 0$), the varying direction of creep deformation in accordance with RSH is not captured. Positive time-dependent deformation appears during creep that is initiated during both unloading and reloading, in accordance with the positiveness of deviatoric stress (i.e., axial stress is greater than radial component). Fig. 9(b) explores the consequence of introducing an assumption that the translation of the RSH surface is driven by both mechanisms (i.e., replacing $\Phi^{\mathrm{II}}$ in Eq. (12) with $\Phi^{\mathrm{I}} + \Phi^{\mathrm{II}}$), such that the hardening of the consolidation surface is related to the plastic volume changes generated by both mechanisms. This simulation shows that adopting a coupled kinematic hardening tends to decrease the magnitude of creep that is aligned with RSH, since the RSH surface moves 'faster' towards the current stress. Despite this difference, both hypotheses regarding the kinematic hardening generate very similar deformation pattern (compare Fig. 8(b) and Fig. 9(b)). Other laboratory tests included in this work do not allow evaluation of whether coupled or uncoupled kinematic hardening is better in replicating actual soil behaviour either, and future experimental work is required.

*Cyclic loading interrupted by stress relaxation*

Hicher (2016) reports a comprehensive study on the time-dependent behaviour of a saturated compacted clay, including strain rate effects (Fig. 10), stress relaxation and creep initiated during primary loading (Fig. 11), and stress relaxation initiated during cyclic loading (Figs. 12 and 13). The proposed model is used to simulate these tests in accordance with parameter set 4 in Table 1. The parameter $M$ is obtained from the effective stress paths corresponding to constant-strain-rate undrained triaxial compression (i.e., Fig. 10(a)), while $\lambda^*$ and $\kappa^*$ are converted from the compression index and recompression index reported by Hicher (2016). The parameter $C$ is found to influence the initial slope of the stress-strain curves for constant-strain-rate compression tests, as shown in Fig. 10(b), and adjusted accordingly to provide the best fit. The parameter $n^{\mathrm{I}}$ is constrained by fitting the sensitivity of constant-strain-rate shear to the change in strain rate, while $\mu^{\mathrm{I}}$ affects the slope of the initial portion of effective stress paths shown in Fig. 10(a).
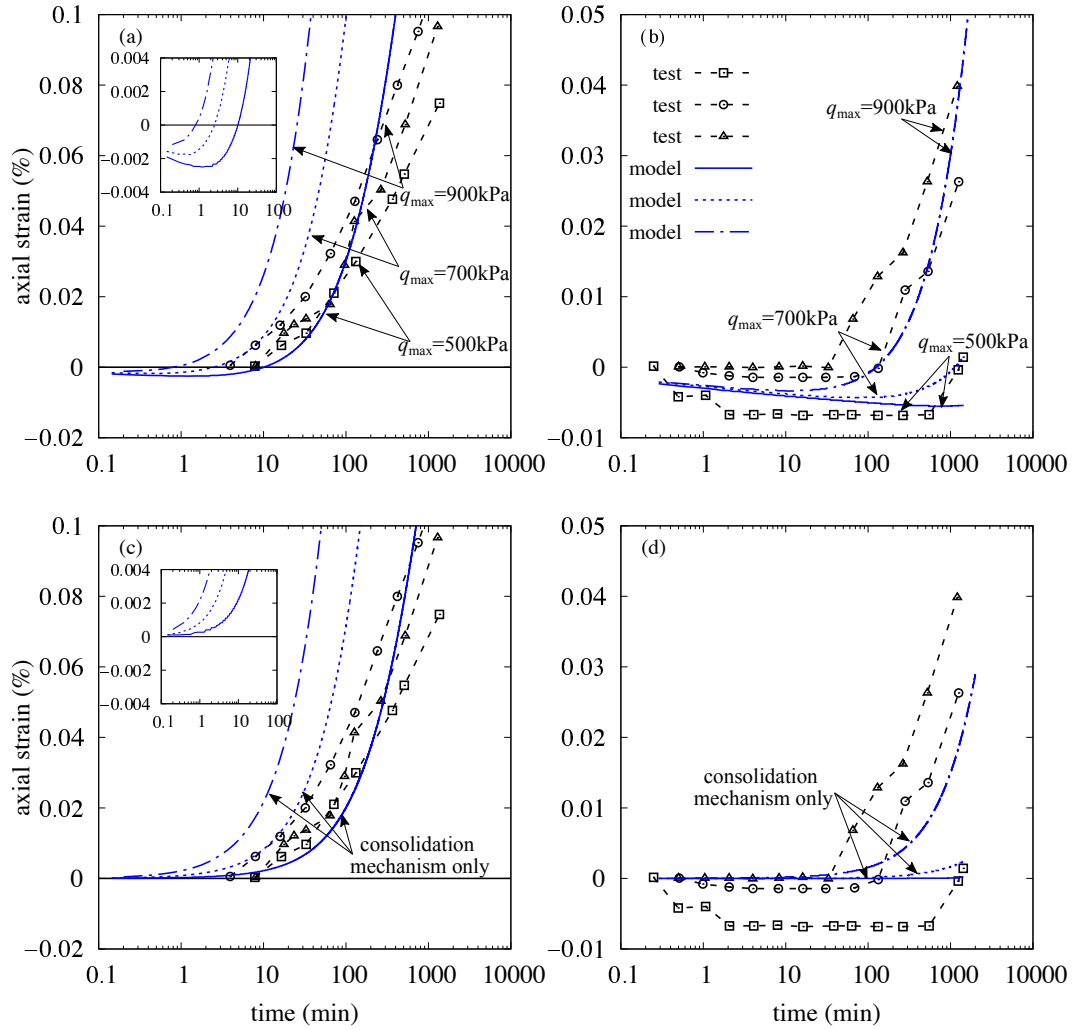
**Fig. 6.** Measured and computed variations of strains with time during (a) creep following $\triangle q = -200$ **kPa stress drop; (b) creep following** $\triangle q = -400$ **kPa stress drop. The label "**$q_{max}$**" indicates the reached deviatoric stresses right before stress drop. Subfigures (c) and (d) repeat the simulations in subfigures (a) and (b), respectively, with only the consolidation mechanism active. The inset figures show the initial portion of the computed creep curves.**
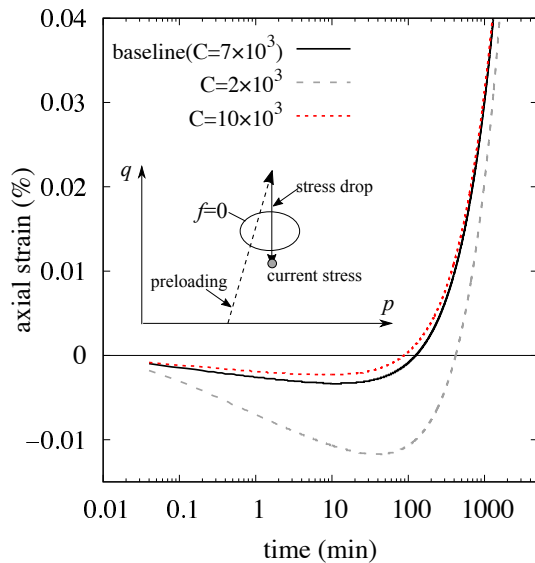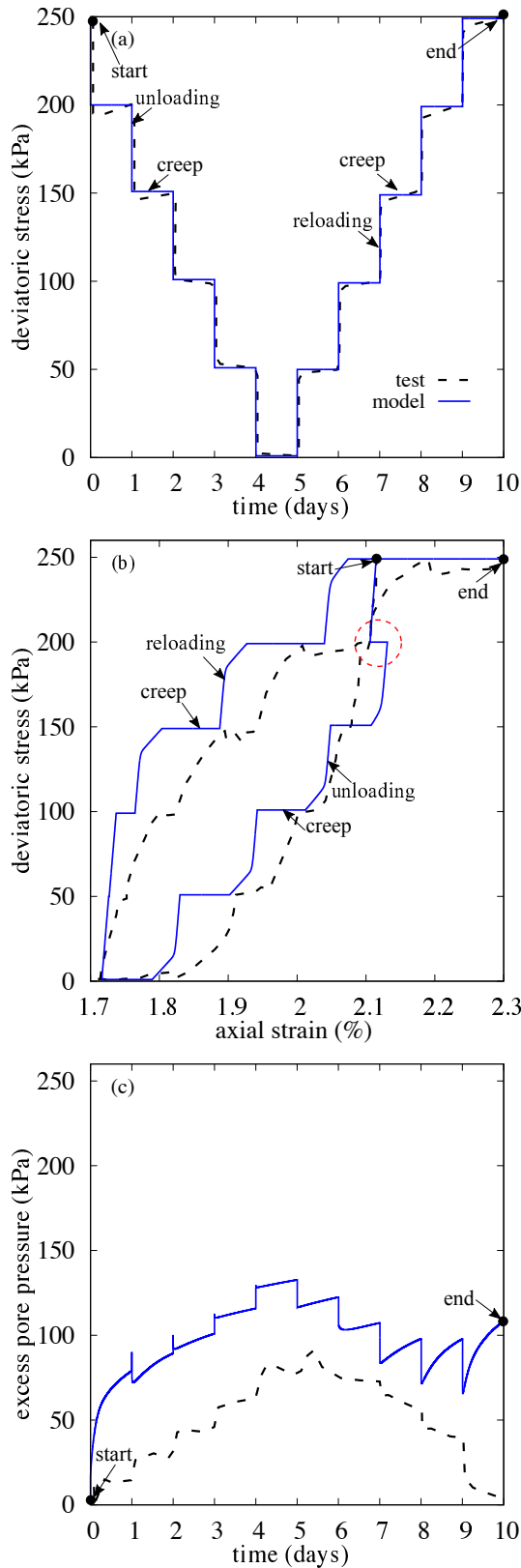


**Fig. 7. Influences of model parameter** $C$**.**

After fixing those parameters, the parameters $n^{II}$ and $\mu^{II}$

are found not to affect significantly the simulation, and they therefore assume the same values as $n^{I}$ and $\mu^{I}$, respectively. The initial values of $p_0$ and $(p_c, q_c)$ are determined following the procedures discussed for the previous two examples.

Test data shown in Figs. 10 and 11 are typical patterns of the viscous behaviour of clayey soils, and the proposed model, like existing models based on single viscoplastic mechanism, can reasonably represent the observed time- and rate-dependence. Figs. 12 and 13 show the time-dependent response in a relatively unconventional testing scheme, where undrained stress relaxation (labelled by "SR" in the figures) is initiated within undrained loading cycles. Similar to the cyclic creep discussed above, these test data show that the stress relaxation, in particular its sign, is affected by the most recent change in effective stress. Those initiated during primary loading (i.e., SR-1) and reloading (i.e., SR-6 and SR-7) exhibit stress reduction, while those initiated during unloading (i.e., SR-2, SR-5, SR-9) are accompanied by stress increase. Moreover, for the stress relaxation initiated following intermediate amounts of unloading (i.e., SR-3, SR-4, SR-8),

**Fig. 8.** Measured and computed response of Formacao de Benfica stiff clay from undrained unloading-reloading cycle with creep stages: (a) temporal variations of deviatoric stress; (b) stress-strain relationships; (c) temporal variations of excess pore pressure. The test scheme consists of a series of unloading and reloading steps executed at an axial strain rate of 0.036 %/min, followed by 24 hrs creep. The undrained condition was maintained throughout the test.
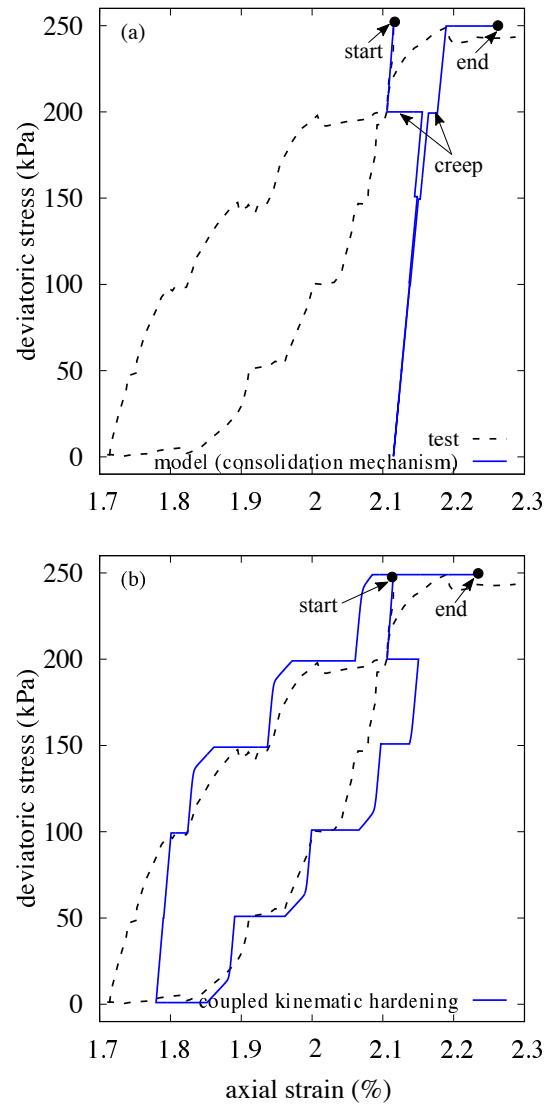


**Fig. 9.** Simulations of cyclic creep test based on different modelling hypotheses: (a) only the consolidation mechanism is active; (b) the kinematic hardening of the RSH surface is driven by two viscoplastic mechanisms.

the stress either decreases from the beginning of the relaxation phase or exhibit a temporary increase before falling again. As noted by Hicher (2016), these observations suggest the existence of multiple viscoplastic mechanisms. Among them, one is related to the primary loading or consolidation and drives the stress decrease during relaxation processes. A second mechanism (called a 'cyclic' mechanism by Hicher (2016)) is mobilized once loading direction changes and generates stress relaxation that is opposite to the most recent stress history. Hicher's multi-mechanism hypothesis is solidified in the Tay creep model. As shown in Figs. 12 and 13, the model successfully replicates the effects on stress relaxation induced by recent change in effective stress. In particular, for SR-4 and SR-8 (see the inset figure in Fig. 13), the model computations clearly reproduce a non-monotonic evolution of stress with time, as observed in the experiment, reflecting the gradual fading of the RSH mechanism. Lastly, Figs. 12 and 13 both highlight that improvements to the preliminary model
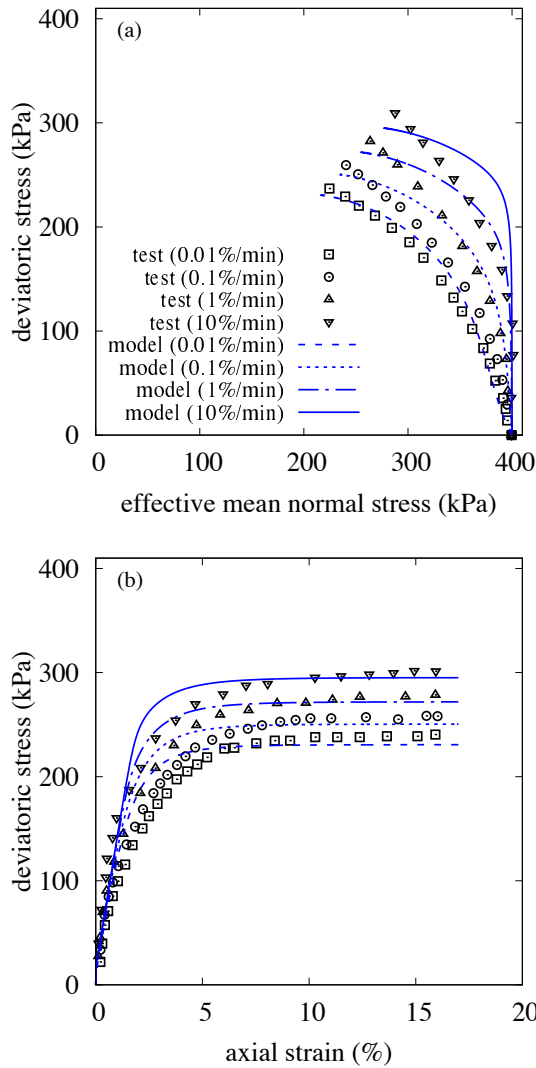
**Fig. 10. Computed and measured response of saturated compacted clay from constant-strain-rate undrained triaxial compression tests: (a) effective stress paths; (b) stress-strain relationships.**

are needed to better quantitatively represent the measured soil response.

DISCUSSION

Using the Tay creep model to interpret the viscous behaviour of soils under complex loading, we show the possibility that multiple mechanisms co-exist and contribute to the irrecoverable, time-dependent deformation of soils. The proposed model, in its present form, includes two mechanisms: consolidation and recent stress history (RSH). The consolidation mechanism could originate microstructurally from the rearrangements of grain contacts or edge-face interactions of clay sheets when the applied stress approaches and surpasses the internal resisting stress linked with soil density. Because the irrecoverable deformation associated with this mechanism reflects the collective response of all particles within the representative elementary volume, it depends on the current stress state (i.e., the homogenization of forces at individual grain contacts) and is less sensitive to the recent
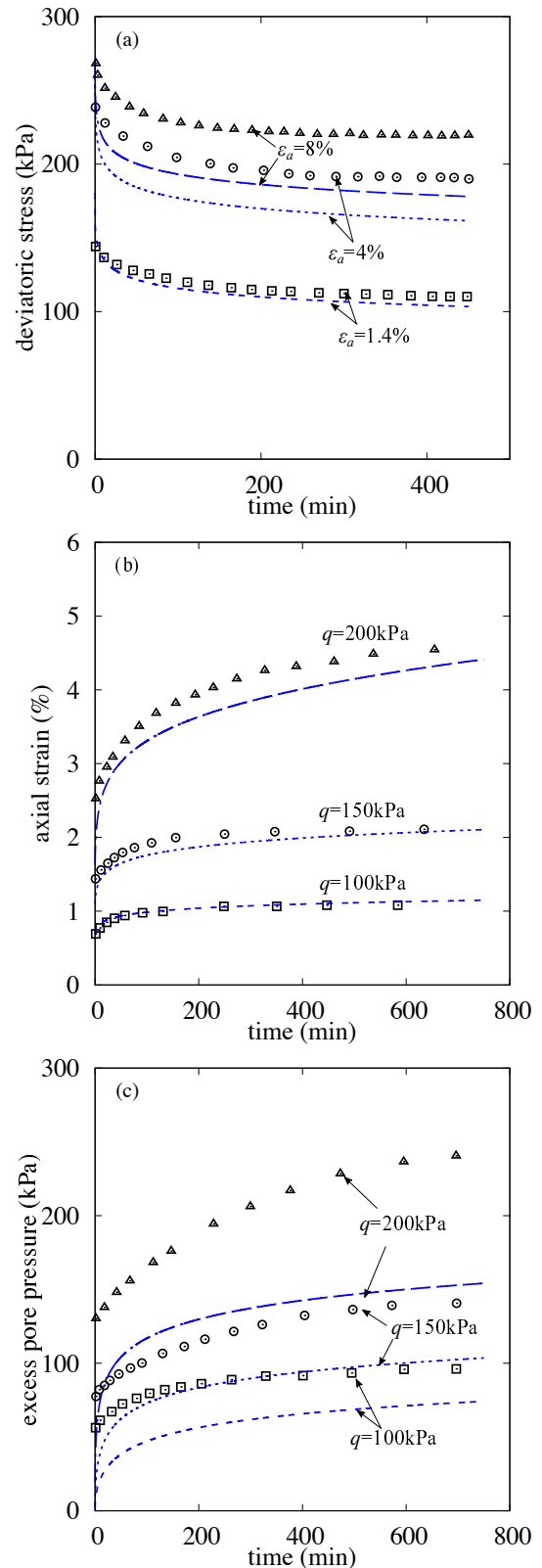
**Fig. 11. Measured and computed (a) undrained stress relaxation and (b,c) undrained creep of saturated compacted clay initiated within monotonic undrained triaxial compression performed at an axial strain rate of 1%/min. The labels "$\epsilon_a$" and "$q$" indicate the strain and stress levels maintained during relaxation and creep, respectively.**

stress history that bring about such a stress state. Differently, the physical origin of the RSH mechanism could be particle
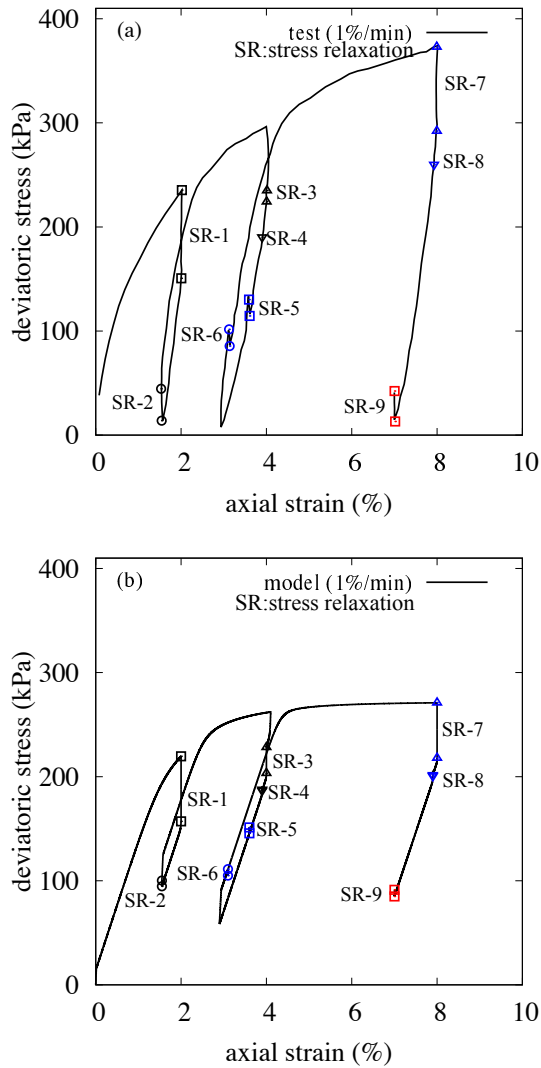
**Fig. 12.** Measured and computed stress-strain relationships of saturated compacted clay from undrained triaxial load cycles with relaxation stages: (a) test data; (b) model computations. Undrained shear is performed at a strain rate of 1%/min and the label "SR" indicates the portions that correspond to stress relaxation.

slips along local 'weak' planes, which require lower activation energy than that of the consolidation mechanism and hence appears evident when the consolidation mechanism is still inactive. Moreover, these local slips, like the movements of dislocations in crystal structure, have kinematic nature and thus are more responsive to the change of stress or straining directions. Between the two mechanisms that have been discussed, there could exist intermediate mechanisms, as represented in Fig. 14(a) by the surfaces located between the consolidation surface ($F = 0$) and the RSH surface ($f = 0$). These mechanisms, similar to the RSH mechanism, are kinematic but requires higher energy or larger stress change to mobilize. Fig. 14(b) shows that these intermediate surfaces are consecutively mobilized as loading proceeds. The physical origin of these intermediate mechanisms could once again be traced to slips but their resisting stresses are higher, much as the energy required for dislocations bypassing long range barriers is higher than that for short range barriers.
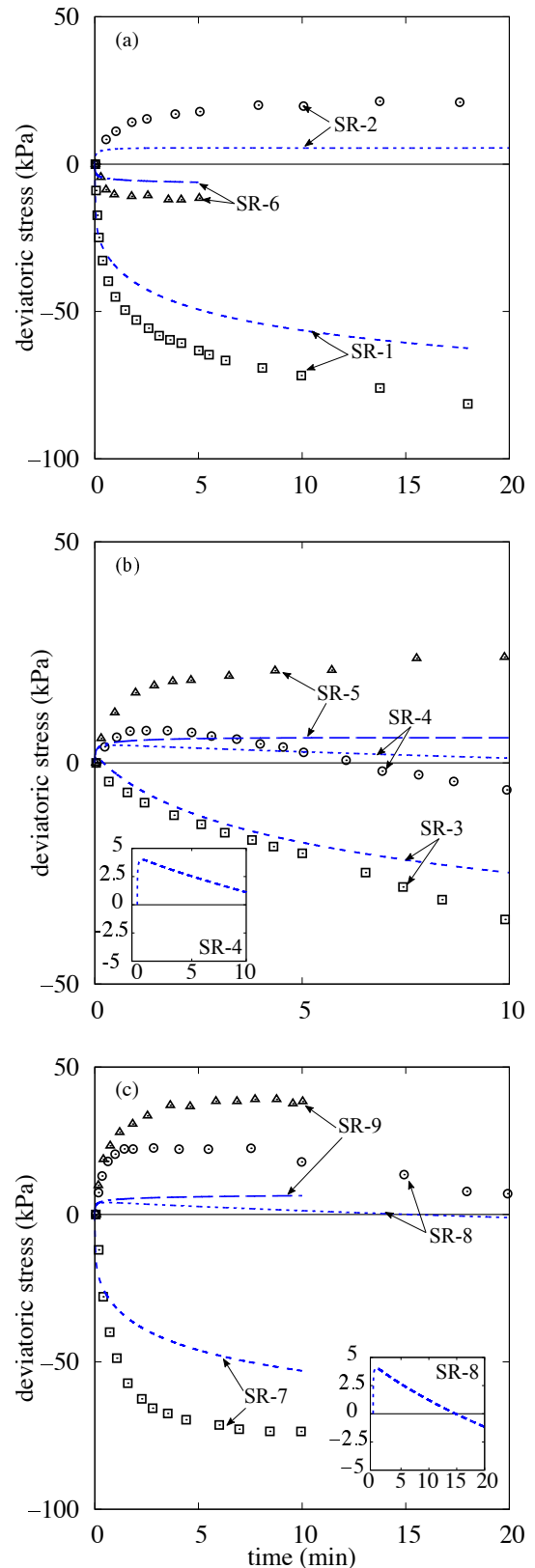
**Fig. 13.** Measured and computed temporal variations of stress deviator during relaxation initiated within load cycles shown in Fig. 12. Inset figures highlight computed stress relaxation and show non-monotonic stress variations.

To provide a basic framework from which extensions are possible, the model formulation has been kept as simple as possible. Mathematically similar relations and surfaces are
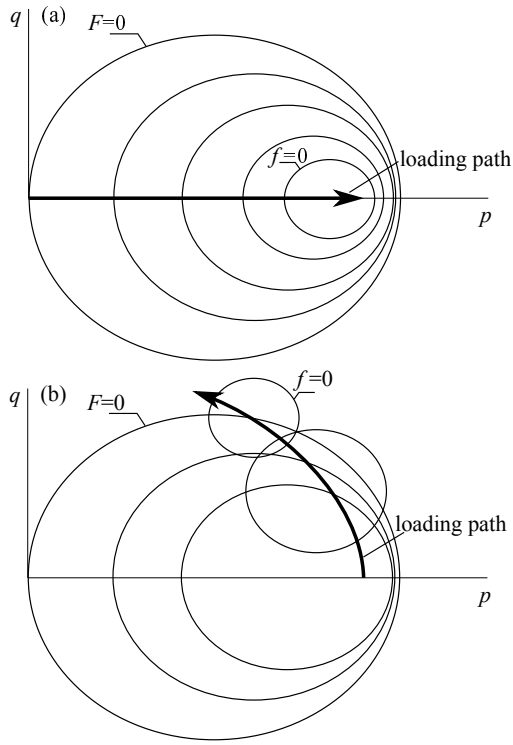
**Fig. 14. Schematics showing the configuration of multi-mechanism surfaces in stress space (a) at the end of consolidation and (b) during subsequent undrained shear.**

employed for the two viscoplastic mechanisms. Nevertheless, we show that such a simple model can reproduce, at least semi-quantitatively, a range of soil creep and rate phenomena that have been observed. Among the employed constitutive hypotheses, some are regarded as essential for replicating well-established behaviour of clay. The combination of the hardening law of Eq. (11) and the hypoelastic model of Eq. (14) is responsible for producing normal compression behaviour and density hardening effects, while the flow rule associated with the consolidation surface ensures that critical state is attained at a unique stress ratio. To simulate sand behaviour, the basic framework of the Tay creep model remains intact, but detailed governing functions should be correspondingly modified. Cone-shaped surfaces are used to quantify the degree of overstress, while dilatancy depends on the current state of confinement and density in relative to critical state. Lastly, shear-hardening should function as the primary hardening mechanism.

## CONCLUDING REMARKS

This work presents a two-mechanism rate-dependent soil model that considers the viscoplastic contributions related to consolidation and recent stress history. These agencies are represented by surfaces in stress space, to which overstresses are measured for computing the rate-sensitive inelastic deformation. Depending on the current stress state with respect to the surfaces and the relative strengths of the overstresses, the two mechanisms interact collaboratively or competitively.

Model simulations show that the interplay is important for replicating soil viscous behaviour under complex loading paths, including (1) the transient reversal of creep direction and stress relaxation direction following stress reversal and (2) the alignment of creep deformation and stress relaxation with the most recent stress history.

## APPENDIX: GENERALISATION OF TAY CREEP MODEL: BEYOND TWO MECHANISMS

The generalisation of the Tay creep model is based on the following strain rate decomposition:

$$\dot{\epsilon}_p = \dot{\epsilon}_p^e + \sum_{i=1}^{n} \dot{\epsilon}_p^{vpi}; \quad \dot{\epsilon}_q = \dot{\epsilon}_q^e + \sum_{i=1}^{n} \dot{\epsilon}_q^{vpi}; \qquad (15)$$

The index $i$ indicates the viscoplastic contribution associated with the $i^{th}$ mechanism. The strain rate for each mechanism could be evaluated by defining their viscosity function $\Phi^i$ and flow direction $(R_p^i, R_q^i)$:

$$\dot{\epsilon}_p^{vpi} = \langle \Phi^i \rangle R_p^i; \quad \dot{\epsilon}_q^{vpi} = \langle \Phi^i \rangle R_q^i \qquad (16)$$

The viscosity function $\Phi^i$ could be a power law (as used in this work), exponential function, or hyperbolic sine function of the degree of overstress:

$$\Phi^i = \Phi^i(b^i) \qquad (17)$$

The variable $b^i$ indicates a measure of the degree of overstress with respect to the particular mechanism surface (see Fig. 14):

$$f^i = f^i(p, q, p^i, p_c^i, q_c^i) = 0 \qquad (18)$$

The internal variable $p^i$ indicates the surface size, while the stress state $(p_c^i, q_c^i)$ gives the centre of the surface. Isotropic and kinematic hardening laws, which respectively control the evolution of the $p^i$ and $(p_c^i, q_c^i)$, should be specified in accordance with the material properties to be reproduced. They can be generally described as

$$dp^i = dp^i(\Phi^1, \Phi^2, ..., \Phi^n, p^i, p_c^i, q_c^i, p, q)$$
$$dp_c^i = dp_c^i(\Phi^1, \Phi^2, ..., \Phi^n, p^i, p_c^i, q_c^i, p, q) \qquad (19)$$
$$dq_c^i = dq_c^i(\Phi^1, \Phi^2, ..., \Phi^n, p^i, p_c^i, q_c^i, p, q)$$

The terms $\Phi^1, \Phi^2, ..., \Phi^n$ suggest the possibility of coupling the hardening of certain mechanisms with the viscosity of remaining mechanisms. Lastly, the viscoplastic flow direction $(R_p^i, R_q^i)$ could be determined by defining the flow potential for each mechanism:

$$R_p^i = \frac{\partial g^i}{\partial p}; \quad R_q^i = \frac{\partial g^i}{\partial q}; \qquad (20)$$

## ACKNOWLEDGEMENTS

## NOTATION

$\dot{\epsilon}_p, \dot{\epsilon}_q$    volumetric and deviatoric strain rates

$\dot{\epsilon}_p^e, \dot{\epsilon}_q^e$    elastic volumetric and deviatoric strain rates

$\dot{\epsilon}_p^{vp}, \dot{\epsilon}_q^{vp}$    viscoplastic volumetric and deviatoric strain rates

$\Phi$    viscosity function

$R_p, R_q$    volumetric and deviatoric components of flow direction

$p, q$    effective mean normal stress and deviatoric stress

$\bar{p}, \bar{q}$    image stress lying on the consolidation surface

$\hat{p}, \hat{q}$    image stress lying on the RSH surface

$M$    critical state stress ratio

$p_0$    internal variable controlling the size of the consolidation surface

$\mu, n$    material constants controlling the viscosity

$\eta$    stress ratio

$\bar{\eta}$    image stress ratio

$p_c, q_c$    center of the RSH surface in triaxial stress space

$r$    material constant controlling the size of the RSH surface

$b_F, b_f$    overstress measure variables

$\lambda^*, \kappa^*$    slope of normal compression line and swelling line in $lnp - lnv$ space

$v$    specific volume

$C$    material constant controlling kinematic hardening

$K, G$    elastic bulk and shear moduli

$\nu$    Poisson's ratio

## REFERENCES

Adachi, T. & Oka, F. (1982). Constitutive equations for normally consolidated clay based on elasto-viscoplasticity. *Soils and Foundations* **22**, No. 4, 57–70.

Al-Tabbaa, A. & Muir Wood, D. (1989). An experimentally based "bubble" model for clay. In *Numerical Models in Geomechanics NUMOG III* (Pietruszczak, S. & Pande, G., eds.), Elsevier Applied Science, pp. 91–99.

Alonso, E. E., Zervos, A. & Pinyol, N. M. (2016). Thermo-poro-mechanical analysis of landslides: from creeping behaviour to catastrophic failure. *Géotechnique* **66**, No. 3, 202–219.

Bardet, J.-P. & Choucair, W. (1991). A linearized integration technique for incremental constitutive equations. *International Journal for Numerical and Analytical Methods in Geomechanics* **15**, No. 1, 1–19.

Besson, J. (2009). Damage of ductile materials deforming under multiple plastic or viscoplastic mechanisms. *International Journal of Plasticity* **25**, 2204–2221, doi:10.1016/j.ijplas.2009.03.001.

Bjerrum, L. (1967). Engineering geology of Norwegian normally-consolidated marine clays as related to settlements of buildings. *Géotechnique* **17**, No. 2, 83–118.

Campanella, R. G. & Vaid, Y. P. (1974). Triaxial and Plane Strain Creep Rupture of an Undisturbed Clay. *Canadian Geotechnical Journal* **11**, No. 1, 1–10.

Cazacliu, B. & Ibraim, E. (2016). Elasto-plastic model for sand including time effect. *Géotechnique Letters* **6**, No. 1, 16–22.

Chaboche, J. L. (2008). A review of some plasticity and viscoplasticity constitutive theories. *International Journal of Plasticity* **24**, No. 10, 1642–1693.

Dafalias, Y. F. (1982). Bounding surface elastoplasticity-viscoplasticity for particulate cohesive media. In *Proc. IUTAM Symposium on Deformation and Failure of Granular Materials*, pp. 97–107.

Dafalias, Y. F. (1986). Bounding Surface Plasticity. I: Mathematical Foundation and Hypoplasticity. *Journal of Engineering Mechanics* **112**, No. 9, 966–987.

Dafalias, Y. F., Manzari, M. T. & Papadimitriou, A. G. (2006). Saniclay: simple anisotropic clay plasticity model. *International Journal for Numerical and Analytical Methods in Geomechanics* **30**, No. 12, 1231–1257.

De Borst, R. (1986). *Non-linear analysis of frictional materials.* Doctoral thesis, Delft University of Technology.

di Prisco, C. & Imposimato, S. (1996). Time dependent mechanical behaviour of loose sands. *Mechanics of Cohesive-Frictional Materials* **1**, No. 1, 45–73.

Gajo, A. & Muir Wood, D. (1999). Severn-trent sand: A kinematic-hardening constitutive model: the p-q formulation. *Géotechnique* **49**, No. 5, 595–614.

Graham, J., Crooks, J. H. A. & Bell, A. L. (1983). Time effects on the stress-strain behaviour of natural soft clays. *Géotechnique* **33**, No. 3, 327–340.

Hicher, P. Y. (2016). Experimental study of viscoplastic mechanisms in clay under complex loading. *Géotechnique* **66**, No. 8, 661–669.

Houlsby, G. T. (1999). A model for the variable stiffness of undrained clay. In *Proc. 2th International Conference on Pre-Failure Deformation Characteristics of Geomaterials: IS Torino 99*, Torino, Italy: Rotterdam: Balkema, pp. 443–450.

Hunsche, U. (1988). Measurements of creep in rock salt at small strain rates. In *The Mechanical Behavior of Salt, 2nd Conference* (Hardy Jr, E. & Langer, M., eds.), Zellerfeld, pp. 187–196.

Kaliakin, V. N. & Dafalias, Y. F. (1990). Theoretical aspects of the elastoplastic-viscoplastic bounding surface model for cohesive soils. *Soils and Foundations* **30**, No. 3, 11–24.

Karstunen, M. & Yin, Z. (2010). Modelling time-dependent behaviour of murro test embankment. *Géotechnique* **60**, No. 10, 735–749.

Kelly, R., Sloan, S., Pineda, J., Kouretzis, G. & Huang, J. (2018). Outcomes of the newcastle symposium for the prediction of embankment behaviour on soft soil. *Computers and Geotechnics* **93**, 9–41.

Kutter, B. L. & Sathialingam, N. (1992). Elastic-viscoplastic modelling of the rate-dependent behaviour of clays. *Géotechnique* **42**, No. 3, 427–441.

Lade, P. V., Liggio, C. D. & Nam, J. (2009). Strain rate, creep, and stress drop-creep experiments on crushed coral sand. *Journal of Geotechnical and Geoenvironmental Engineering* **135**, No. 7, 941–953.

Leoni, M., Karstunen, M. & Vermeer, P. (2008). Anisotropic creep model for soft soils. *Géotechnique* **58**, No. 3, 215–226.

Leroueil, S., Kabbaj, M., Bouchard, R. & Tavenas, F. (1985). Stress—strain—strain rate relation for the compressibility of sensitive natural clays. *Géotechnique* **35**, No. 2, 159–180.

Maranha, J. R., Pereira, C. & Vieira, A. (2016). A viscoplastic subloading soil model for rate-dependent cyclic anisotropic structured behaviour. *International Journal for Numerical and Analytical Methods in Geomechanics* **40**, No. 11, 1531–1555.

Matsushita, M., Tatsuoka, F., Koseki, J., Cazacliu, B., Di Benedetto, H. & Yasin, S. J. M. (1999). Time effects on the pre-peak deformation properties of sands. In *Proc. 2th International Symposium on Pre-Failure Deformation Characteristics of Geomaterials: IS Torino 99*, Torino, Italy: Balkema: Rotterdam, pp. 681–689.

Mróz, Z. (1967). On the description of anisotropic workhardening. *Journal of the Mechanics and Physics of Solids* **15**, 163–175.

Muir Wood, D. (2004). *Geotechnical modelling*. CRC Press.

Oldecop, L. A. & Alonso, E. (2007). Theoretical investigation of the time-dependent behaviour of rockfill. *Géotechnique* **57**, No. 3, 289–301.

Perzyna, P. (1963). The constitutive equations for rate sensitive plastic materials. *Quarterly of Applied Mathematics* **20**, No. 4, 321–332.

Pham Van Bang, D., Di Benedetto, H., Duttine, A. & Ezaoui, A. (2007). Viscous behaviour of dry sand. *International Journal for Numerical and Analytical Methods in Geomechanics* **31**, No. 15, 1631–1658.

Prévost, J. (1977). Mathematical modelling of monotonic and cyclic undrained clay behaviour. *International Journal for Numerical and Analytical Methods in Geomechanics* **1**, No. 2, 195–216.

Puzrin, A. M. & Houlsby, G. T. (2004). On the non-intersection dilemma in multiple surface plasticity. *Géotechnique* **51**, No. 4, 369–372.

Roscoe, K. H. & Burland, J. B. (1968). On the generalised stress–strain behaviour of 'wet' clay. In *Engineering plasticity*, pp. 535–609.

Rouainia, M. & Muir Wood, D. (2000). A kinematic hardening constitutive model for natural clays with loss of structure. *Géotechnique* **50**, No. 2, 153–164.

Schofield, A. & Wroth, C. (1968). *Critical State Soil Mechanics*. McGraw-Hill.

Sheahan, T. C., Ladd, C. C. & Germaine, J. T. (1996). Rate-dependent undrained shear behavior of saturated clay. *Journal of Geotechnical Engineering* **122**, No. 2, 99–108.

Shi, Z., Hambleton, J. P. & Buscarnera, G. (2019). Bounding surface elasto-viscoplasticity: A general constitutive framework for rate-dependent geomaterials. *Journal of Engineering Mechanics* **145**, No. 3, 04019002.

Suklje, L. (1957). The analysis of the consolidation process by the isotaches method. In *Proceedings of the 4th International Conference on Soil Mechanics and Foundation Engineering*, vol. 1, London, pp. 200–206.

Tamagnini, C., Viggiani, G., Chambon, R. & Desrues, J. (2000). Evaluation of different strategies for the integration of hypoplastic constitutive equations: Application to the cloe model. *Mechanics of Cohesive-frictional Materials* **5**, No. 4, 263–289.

Tavenas, F., Leroueil, S., La Rochelle, P. & Roy, M. (1978). Creep behaviour of an undisturbed lightly overconsolidated clay. *Canadian Geotechnical Journal* **14**, 402–423.

Vermeer, P. & Neher, H. (1999). A soft soil model that accounts for creep. In *Proc. Beyond 2000 in Computational Geotechnics - 10 Years of PLAXIS International*, Balkema, Rotterdam, pp. 1–13, doi: 10.1201/9781315138206-24.

Yuan, Y. & Whittle, A. J. (2018). A novel elasto-viscoplastic formulation for compression behaviour of clays. *Géotechnique* **68**, No. 12, 1044–1055.

Zhu, H. & Randolph, M. F. (2011). Numerical analysis of a cylinder moving through rate-dependent undrained soil. *Ocean Engineering* **38**, No. 7, 943–953.